Zachary B. Towner,[1] Kyle V. Smith,[2] Sachin R. Shinde,[2]
Santosh B. Narasimhachary,[3] Richard W. Neu,[1,4]
Christopher L. Muhlstein,[4] and Ashok Saxena[4,5]

Evolution of Creep Deformation near Tips of Sharp Notches and Cracks in CM247LC-DS Ni-Base Superalloy

Citation

Z. B. Towner, K. V. Smith, S. R. Shinde, S. B. Narasimhachary, R. W. Neu, C. L. Muhlstein, and A. Saxena, "Evolution of Creep Deformation near Tips of Sharp Notches and Cracks in CM247LC-DS Ni-Base Superalloy," in *Advances in Accelerated Testing and Predictive Methods in Creep, Fatigue, and Environmental Cracking*, ed. K. Nikbin, Z. Wei, and S. Kalluri (West Conshohocken, PA: ASTM International, 2023), 63–82. http://doi.org/10.1520/STP164320210099[6]

ABSTRACT

Finite element analyses were performed for varying crack tip or notch geometries and temperatures in C(T) specimens of CM247LC-DS Ni-base superalloy used in gas turbine blades to understand the accumulation of creep strains at notches. The constitutive models used considered elastic-primary-secondary creep deformation behavior. Simulations were performed under 2D plane stress, 2D plane strain, and 3D conditions for temperatures of 750°C, 850°C, and 950°C.

The estimated load-line displacements as a function of time from finite element analyses and from analytical expressions were validated using results from experiments conducted on notched and fatigue precracked C(T) specimens. Differences in the development of the creep zone size due to the notch tip geometry diminish in time under plane stress conditions, but they do not for plane strain conditions. Over short periods of time, small-scale creep plays a significant role in the evolution of the notch tip creep zones. The 3D analysis results show that creep zones grow at a faster rate on the surface of the specimen than in the mid-thickness region, and these differences are exacerbated as the notch root radius decreases. This work can potentially be the basis for formulating a theory for creep crack formation from notches in CM247LC-DS alloys.
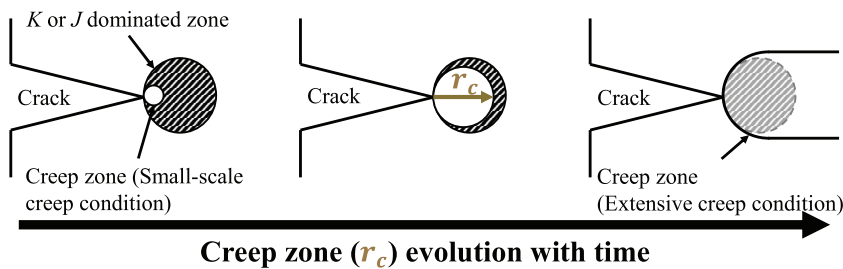
Introduction

Creep is an important design consideration for hot-section gas turbine blades because components are subjected to high-temperatures and sustained loads during service. Designers have incorporated innovative techniques to extend the design life of blades through temperature-mitigation strategies such as machining cooling holes in the blades. However, such geometric discontinuities act as stress concentrators and become the life-limiting factor because they are locations for crack initiation due to creep deformation. When cracks form, time-dependent fracture mechanics methodologies for service life estimations become an attractive approach. Prior studies[1–5] have shown that the elastic stress field ahead of a sharp crack relaxes due to creep accumulation. Intuitively, this region evolves with time for a stationary crack, as idealized in figure 1. This region of stress relaxation, or the creep process zone (r_c), has been a crucial attribute of time-dependent fracture mechanics because the continuum field quantities in this zone directly influence the actual fracture process. Direct comparisons of the creep zone evolution for a sharp

FIG. 1 Idealized creep zone evolution in time.

K or J dominated zone

Crack

Creep zone (Small-scale creep condition)

Crack

r_c

Crack

Creep zone (Extensive creep condition)

Creep zone (r_c) evolution with time

crack geometry versus an acute notch of finite radius (i.e., before a crack is present) have not been explicitly reported in the literature. Furthermore, since the creep zone size cannot be directly measured in experiments, finite element analyses (FEA) are necessary for such investigations.

Ni-base superalloys are used in hot-section turbine blades because they maintain excellent strength and corrosion resistance at elevated temperatures. Directional solidification (DS) or single crystal (SX) casting techniques produce parts with anisotropic material properties. Aligning the material's microstructural orientation with the best mechanical properties with the direction of high applied force improves turbine blade performance. However, correctly modeling the material behavior inevitably becomes more complex, and this complexity can delay early-stage design evaluations. Simpler constitutive models lend themselves to faster implementation.

Experimental and finite element investigations were performed in tandem to provide immediate insights into the material behavior preceding the onset of crack extension for two different crack tip geometries: a sharp crack and an acute notch of finite radius. Ideal representations of these geometries are shown in figure 2. This paper explores the efficacy of a simple constitutive model for capturing the high-temperature creep behavior of a directionally solidified (DS) Ni-base superalloy. The influence of crack tip geometry on far-field measurements versus local phenomena is assessed to show the limitations of current techniques. The role of varying crack tip geometries and temperatures on the evolution of the creep zone size preceding the onset of creep crack growth is discussed and the dependence of the creep zone shape on the stress state is qualitatively explored.

Material

CM247LC-DS used in this study is a cast, DS, Ni-base superalloy with a chemical composition similar to one used by Harris, Erickson, and Schwer;[6] the composition is presented in table 1. Derived from the base MAR-M247 chemistry, this alloy was

FIG. 2 Sharp crack versus acute notch geometries.
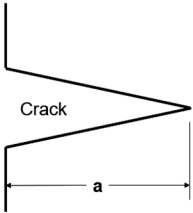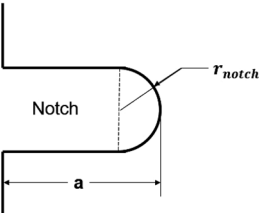

	Crack	Notch
Idealization	Crack (a)	Notch r_{notch} (a)
Physical Feature	Fatigue precrack	Electric discharge machining
Finite Element Model	Crack tip elements	Quadrilateral elements

TABLE 1   Typical chemical composition of the DS Ni-base superalloy used in this study (wt. %)

Al	5.6	Cr	8.1	Ta	3.2
B	0.015	Hf	1.4	Ti	0.7
C	0.07	Mo	0.5	W	9.5
Co	9.2	Ni	Balance	Zr	0.015

designed specifically to minimize grain boundary cracking as well as to optimize the carbide size and distribution and the microstructural stability of the alloy. A two-step solid solutioning treatment followed by two-step aging breaks down and redistributes the strengthening precipitates and the carbides. The microstructure consists of two primary phases: the austenitic γ-phase, which has a face-centered cubic (FCC) structure consisting of nickel, and the γ'-phase, an ordered L_{12} structure of Ni3(Al, Ti) where the nickel fills the octahedral sites of the FCC-type structure. These form a solid solution of predominantly γ' intermetallic precipitates ($> 60\%$ by volume) in the γ matrix. The average γ' precipitate size is $\sim 0.5\,\mu m$, although variations in processing can change the particle size by $+0.4\,\mu m/{-}0.2\,\mu m$. During the solidification process, columnar dendritic structures of γ and γ' form and additional alloying elements are segregated to the interdendritic regions. Figure 3 shows the columnar grain structure of this superalloy.

Erickson, Harris, and Schwer[7] noted the improved creep-rupture life of CM247LC-DS over the base MAR-M247 superalloy due to the increased effective volume fraction of γ', even after a single heat treatment; the goal of the second heat treatment was then to achieve a $> 90\%$ eutectic solutioning in the final alloy.[7] Figure 4 shows the creep behavior of CM247LC-DS at various temperatures and load levels in the longitudinal direction. At lower temperatures, significant primary creep occurs when the applied stress is high. Deformation in the primary creep regime is found to be generally homogeneous and results from shearing of the γ' precipitates, allowing

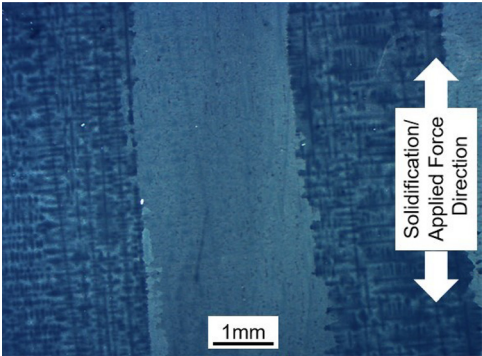**FIG. 3**   Typical columnar grain structure of CM247LC-DS.

FIG. 4   Longitudinal creep behavior normalized by the maximum creep strain
measured at various temperatures, compiled by experiment and literature at
(*A*) 750°C, (*B*) 850°C, and (*C*) 950°C. (Note: 700 MPa at 750°C is the only data
set from the literature presented here.[10]) Note the diminished role of the
primary creep deformation at higher temperatures.
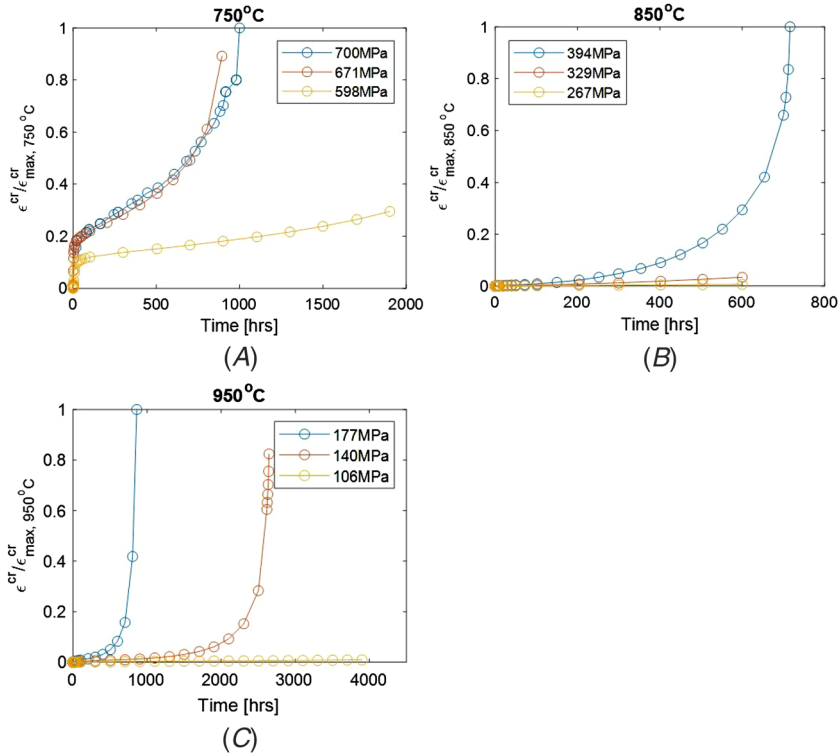
for more uniform deformation. At higher temperatures, the primary creep disappears,
and the secondary and tertiary creep regimes become dominant. This change is due
to the softening of the γ matrix and the dissolving of finer γ' precipitates. Inspection
of creep-tested CM247LC-DS samples reveals that damage occurs on both the surface
and in the bulk of samples. These observations are similar to those of Reed,[8] which
were noted for SX creep behavior. Scanning electron microscope (SEM) observations
show that creep cavitation occurs at grain boundaries and carbides, while oxidation
occurs on the surface leading to crack formation.[9]

Experimental Procedure

A series of creep crack growth (CCG) experiments were conducted following
ASTM E1457-19, *Standard Test Method for Measurement of Creep Crack Growth*

Times in Metals (superseded),[11] on compact type (C(T)) samples of CM247LC-DS, with typical dimensions given in **figure 5**. Tests were conducted on samples containing either small-radius electrical discharge machined (EDM) notches or sharp cracks generated by fatigue precracking. Cracked samples were also tested with side grooves to constrain the crack path through the sample and to create a more uniform state of stress across the crack front. Samples were machined so that the crack plane was perpendicular to the direction of solidification.

The typical experimental setup is shown in **figure 6**. The desired specimen temperatures were achieved and maintained with a clamshell furnace and West 6100 + temperature controller. Specimen temperature was continuously monitored via K-type thermocouples welded to the specimen at the locations indicated in **figure 5**, and the temperature profile on the projected crack plane was maintained within the specifications of the standard for the duration of each experiment. Load-line displacement was measured either at the knife edges of the sample ($V_{LLD,KE}$), at the lever arm of the SATEC dead-weight creep frame ($V_{LLD,LA}$), or both. $V_{LLD,KE}$ was transferred out of the furnace via a custom rod-in-tube extensometer to a super linear variable capacitive transducer; $V_{LLD,LA}$ was measured with a dial gauge.

FIG. 5   Standard dimensions in mm of the C(T) samples tested in this study. Initial starter notch or crack length, *a*, varied between 0.35 < a/W < 0.45. Circles are locations of thermocouples. Squares are contact points of the rod-in-tube extensometer. Cross-hatched triangles are locations of constant current input leads. Solid triangles are direct current (DC) potential drop output lead locations (note the reference lead location in the location remote from the crack tip).
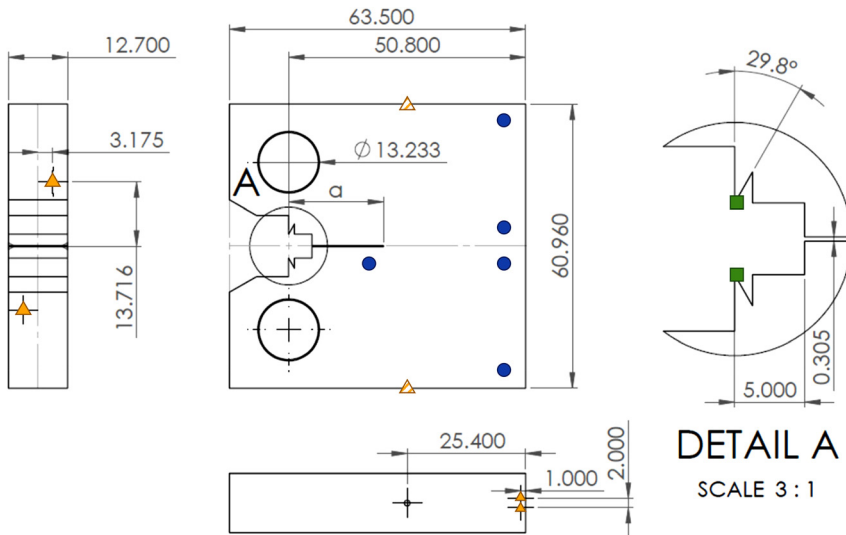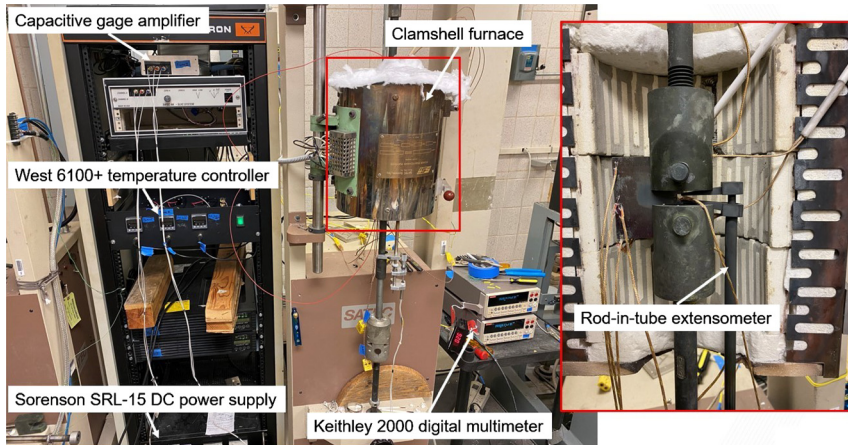
FIG. 6   Typical experimental setup for CCG testing.

The crack length was monitored via the DC electrical potential drop technique. A low-ripple Sorensen SRL 10-25 DC power supply provided nominally 5A constant current to the sample. The potential drop across the crack mouth opening, V_{EPD}, was either amplified via an Omega III amplifier and routed to the Measurement Computing USB-1608G data acquisition device (DAQ) or measured directly via a Keithley 2000 digital multimeter. A reference line potential drop signal, V_{EPDref}, from the corner remote from the crack tip was also recorded to monitor system changes with time. Temperature and $V_{LLD,KE}$ signals were also routed to the DAQ. Data were automatically recorded at 0.5Hz frequency via TracerDAQ Pro software or by a custom LabVIEW program.

Following the recommendations of E1457-19, a plot of V_{EPD} versus V_{LLD} was used to identify the onset of CCG. After the initial downward or constant trend in the V_{EPD} versus V_{LLD} data, the V_{EPD} began to rise when the crack began to form. The time associated with this point was used as the crack formation time and subsequently the maximum simulation time limit in the FEA.

Finite Element Analyses

CONSTITUTIVE MODELING

Empirical and physics-based constitutive models have been proposed that capture various attributes of creep behavior in Ni-base superalloys and that can capture a range of complexity. However, simpler models are preferred that enable faster implementation during component analysis. The stress and temperature dependence of creep deformation can be decoupled by asserting that the creep rate is a product of separable functions of temperature and stress. Under isothermal

conditions, it simplifies to creep rate behavior that is dependent only on stress under steady-state conditions. These stress functions typically follow power-law, exponential law, or hyperbolic sine law formulations. Classical examples of such models include those proposed by Norton[12] and Garofalo.[13] Bassani and McClintock,[2] Riedel,[14] and Saxena[15] have incorporated variations of these simple models in analyses of creep deformation near crack tips.

CM247LC-DS superalloy was idealized using an orthotropic elastic[16] and isotropic creep[17] material model. The elastic modulus and Poisson's ratio are needed for determining the orthotropic elastic material properties. Tensile test data collected at the temperatures of interest (750°C, 850°C, 950°C) provided the elastic modulus in the longitudinal (i.e., parallel to the DS orientation) and transverse directions. The Poisson's ratios in the longitudinal and transverse directions were assumed to be constant, with temperature following Neal.[18] Prebuilt in ABAQUS is the Darveaux creep model,[19] a phenomenological creep model capable of capturing both primary and secondary, or steady-state, creep behaviors: equations (1) and (2), respectively.

$$\dot{\bar{\varepsilon}}^{cr} = \dot{\bar{\varepsilon}}_s^{cr} \left[1 + \epsilon_T H exp\left(-H\dot{\bar{\varepsilon}}_s^{cr} t\right)\right] \qquad (1)$$

$$\dot{\bar{\varepsilon}}_s^{cr} = C_{ss}[sinh(\alpha\tilde{\sigma})]^n exp\left(-\frac{Q}{R(\theta - \theta_z)}\right) \qquad (2)$$

where:

$\dot{\bar{\varepsilon}}^{cr}$ = the uniaxial equivalent creep strain rate,

$\dot{\bar{\varepsilon}}_s^{cr}$ = the uniaxial equivalent steady-state creep strain rate,

ϵ_T = the transition strain from primary to secondary creep stage,

H, C_{ss}, α, n = temperature-dependent material parameters obtained from regression of the creep deformation data,

$\tilde{\sigma}$ = the von Mises stress,

Q = the activation energy,

R = the universal gas constant,

θ = the temperature in degrees K, and

θ_z = the user-defined absolute zero.

Creep strain versus time data were used in determining Darveaux model[19] parameters, which are listed in table 2. Only primary and secondary creep strain behaviors are of interest to this work because subsequent analyses assessed stress and strain field evolution behavior ahead of stationary cracks and notches.

The secondary creep model parameters were determined first for a given temperature. Steady-state creep strain rate and transition strain, ϵ_T, were determined by a linear least-squares regression of creep strain versus time data points, which yielded $R^2 > 0.999$ around the minimum creep strain rate following the procedure of Darveaux.[19] The variable α was arbitrarily chosen, and C_{SS} and n were determined via least-squares fit of steady-state creep strain rate versus $sinh(\alpha\tilde{\sigma})$. Since C_{ss}, α, n were temperature dependent and subsequent simulations were carried out under

TABLE 2 Material model parameters for the DS Ni-base superalloy.

Temperature (°C)	750	850	950
E_L (MPa)	99,049.2	92,407.6	85.239.5
E_T (MPa)	139,188.0	129,288.0	118,303.0
v_L		0.2	
v_T		0.4	
C_{SS} (1/hr)	1.440×10^{-9}	7.590×10^{-7}	3.059×10^{-5}
α (1/MPa)		5.0×10^{-3}	
n	4.012	2.912	6.406
Q/R		0.0	
θ_Z (°K)		0.0	
ϵ_T (mm/mm)	2.245×10^{-2}	1.680×10^{-4}	4.460×10^{-4}
B	6270	100.0×10^3	136.0×10^2

isothermal conditions to match experiments, the Q/R coefficient was assumed to be constant (in this case, set to zero) and any effects are assumed to be incorporated in C_{SS}. The model-predicted $\dot{\bar{\epsilon}}_s^{cr}$ for each load level was used in conjunction with the integrated form of equation (1) to fit the creep strain versus time data in the primary and secondary creep regimes, which yielded H.

Figure 7 shows the ability of the constitutive model to represent the primary and secondary creep behavior of CM247LC-DS. The figure shows that the model adequately followed the experimental data trends for subsequent analyses. It seems to be less accurate at 750°C, especially for higher stress levels, compared to higher temperatures at 850°C and 950°C.

MODEL GEOMETRY

The C(T) sample shown in figure 8 was modeled and analyzed with ABAQUS 2020. 2D and 3D models were created for verification and validation of subsequent results. The initial crack length, which varied to match a given experiment, was modeled as either an infinitely sharp crack or as an acute notch of finite radius, r_{notch}, which varied from 0.1 to 1.0 mm. Element sizes ranged from 0.02 W to 0.1 r_{notch}, where W is the ASTM-defined specimen width. 2D models consisted of either plane stress (PS) or plane strain (PE) elements—CPS8R or CPE8R, respectively—and 3D models consisted of C3D8R elements. In the 2D model, half of the sample was modeled due to symmetry and the thickness was specified. In the 3D model, quarter symmetry was utilized. Symmetric boundary conditions were applied to (1) the region of the projected crack plane and (2) the node (2D model) or the edge (3D model) of the intersection of the projected crack plane and the back face of the sample. The load-bearing surface of the pin hole (edge in the 2D model, face in the 3D model), which was between $60° < \theta < 120°$ on the pin hole,[20] was constrained to the geometric node at $\theta = 90°$ through continuum-distributed coupling; the simulated pin load was applied as a concentrated force to this node.

FIG. 7   Verification of constitutive model parameters to fit experimental primary and secondary creep strain versus time data for CM247LC-DS at (*A*) 750°C, (*B*) 850°C, and (*C*) 950°C.
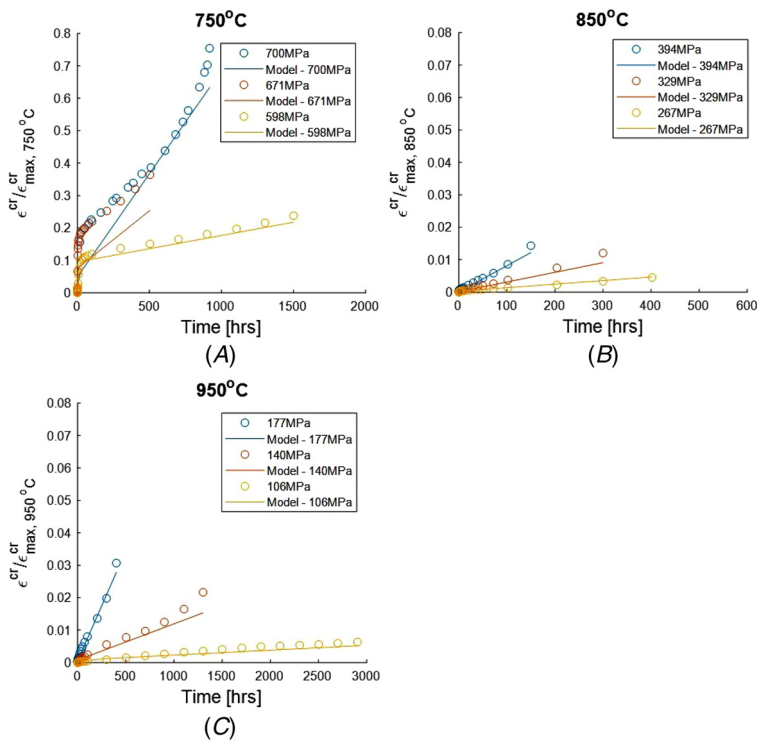

FIG. 8   Typical geometric model configuration on the 2D model geometry. (*A*) Symmetric boundary conditions applied on projected crack plane (dashed edge) and restricted X motion applied at solid node. Applied concentrated force at cross-hatched node with continuum-distributed coupling on the upper bearing surface (solid edge). $V_{LLD,KE}$ measured from the location indicated in (*B*). Element refinement increased near the crack tip or notch root.
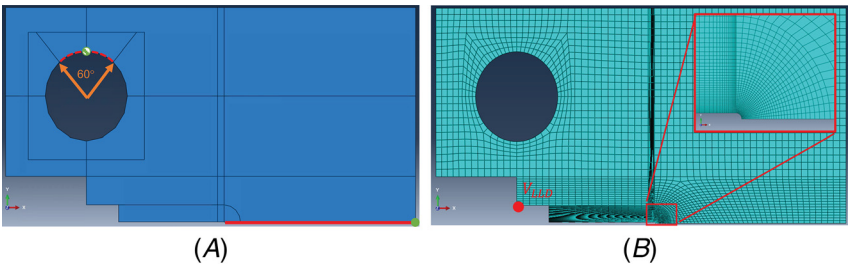
A simple elastic analysis verified the performance of the geometric model. The shape factor for a C(T) sample can be extracted from the sharp crack model by varying either the applied force or the crack length while keeping the other constant. Figure 9 compares the value of the shape factor generated from a 2D PS finite element model for varying a/W to the shape factor from the K-solution for a C(T) sample presented in ASTM E1457-19;[11] the good agreement between the two is evident.

FINITE ELEMENT ANALYSIS PROCEDURE

For simulating the experimental procedure of a CCG test, the FEA procedure consisted of two steps: a short, viscous loadup and a viscous hold period. In ABAQUS, viscous steps allow for creep strain to occur in each step. The loading duration was minimal to ensure that elastic deformation dominated time-dependent deformation. The hold period was set equal to the time prior to crack formation observed in the experiment (i.e., positive change in the slope of the V_{EPD} versus V_{LLD} plot).

Results and Discussion

The efficacy of the constitutive law in representing material behavior can be evaluated by comparing experimental measurements remote from the crack tip to predictions from FEA, analytical solutions, or both where applicable. Once the FEA results are validated, the stress and strain distributions as well as the evolution of the crack tip creep zone size and shape from the FEA can be examined with high confidence. An analytical equation for predicting load-line displacement due to creep measured at the knife edge of a sharp crack C(T) sample[15] is presented in equation (3). This equation was derived using a simple elastic plus secondary

FIG. 9 Geometric model verification via extraction of shape factor polynomial for a C(T) sample.
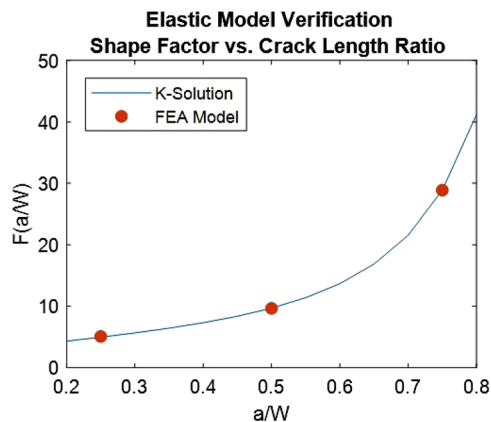
power-law creep[12] constitutive model. It is acceptable for comparison with 850°C or 950°C finite element simulation results and the experimental data because the influence of primary creep is not as significant as at 750°C. The Darveaux model does not lend itself to an analytical derivation for load-line displacement at the knife edge due to creep.

$$\dot{V}_{ssc} = \frac{4\alpha(1-\nu^2)}{E(n-1)} \beta F_{cr} \left(\frac{P}{B}\right)^3 \frac{F^4}{W^2} (EA)^{2/(n-1)} t^{-(n-3)/(n-1)} \quad (3)$$

where:
$\dot{V}_{ssc}$ = the deflection rate at the load line due to small-scale creep,
α, β = constants,
A, n = the Norton power-law creep coefficient and exponent, respectively,
P = the applied force,
B = the sample thickness,
F = the value of the shape factor for a given a/W,
W = the remaining ligament length,
t = time, and
F_{cr} = an angular function dependent on the creep exponent and the angle from crack tip.[1]

Figure 10A compares experimental load-line displacement versus time data from an 850°C CCG test on a 20% side-grooved sample with a sharp precrack under $K_0 = 50$ MPa$\sqrt{m}$ to analytical (equation [3]) and 2D FEA predictions. The close agreement between the experimental data and the analytical and finite element predictions supports the notion that subsequent analyses of the notch root and crack

FIG. 10   Plot comparing analytical and finite element predictions of $V_{LLD,KE}$ versus time to experimental data. Experiment and simulation conditions are defined in the plot titles of (*A*) and (*B*).
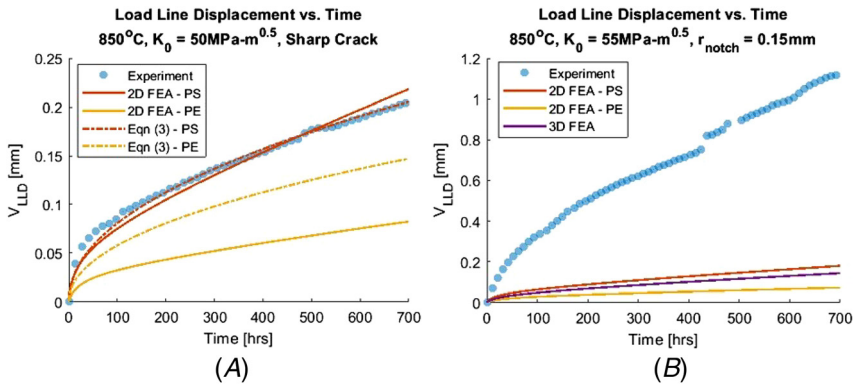
tip stress and strain fields are valid. The 2D PS FEA and analytical predictions of load-line displacement match more closely to the experimental data than the 2D PE predictions. This fact suggests that PS modeling may be more useful for predicting displacements remote from a sharp crack than PE modeling, which designers may be inclined to pursue given the thickness of the sample. Figure 10*B* compares experimental data to 2D and 3D FEA predictions of a different 850°C CCG test on a plane-sided sample with an acute notch and subjected to $K_0 = 55$ MPa$\sqrt{m}$. As expected, the predicted load-line displacement from the 3D model lies between the bounds of the 2D PS and PE models, although the 3D model predictions lean closer to the PS bounding case. However, the FEA predictions underpredicted the far-field load-line displacement observed in this experiment. The large difference between the experiment and the predictions shows the influence the notch has on the actual far-field behavior of this material. However, the exacerbation of the difference was likely spurred by incremental slipping of the capacitive transducer in the rod-in-tube extensometer assembly throughout the experiment; an example of this occurrence is exemplified by the jump in the load-line displacement at ∼425 hr. Despite this difference, subsequent analyses of stress and strain fields near the crack tip remain pertinent.

For a given crack length and applied load, figure 11 shows that reducing r_{notch} decreases the amount of load-line displacement observed in time. However, the difference in the far-field measurement is small (∼10^1μm). Thus, it can be concluded that the load-line displacement, which is used for creep zone size estimates, inadequately differentiates crack tip geometry. This observation has been similarly noted by Bassani and McClintock,[2] further supporting this conclusion. Figure 11 also shows

FIG. 11 Comparison of predicted $V_{LLD,KE}$ versus time for various r_{notch} values generated from 3D finite element models.
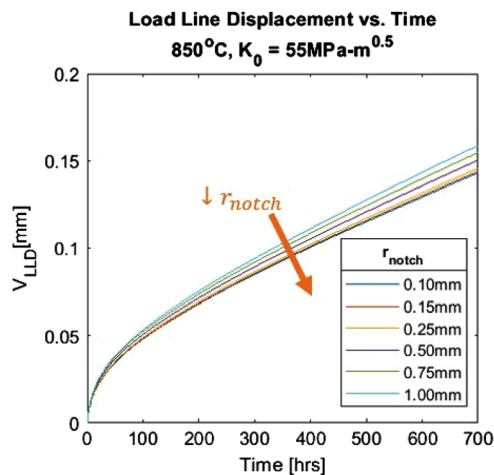
FIG. 12   Summarizing plots from a series of 2D, 850°C simulation under $K_O = 55MPa\sqrt{m}$ conditions. (*A*) Equivalent stress versus distance from the notch root, r; PS conditions. The inlaid figure specifies the location where *r* is measured. (*B*) Equivalent stress versus distance from the notch root; PE conditions. (*C*) Equivalent creep strain versus distance from the notch root; PS conditions. (*D*) Equivalent creep strain versus distance from the notch root; PE conditions.
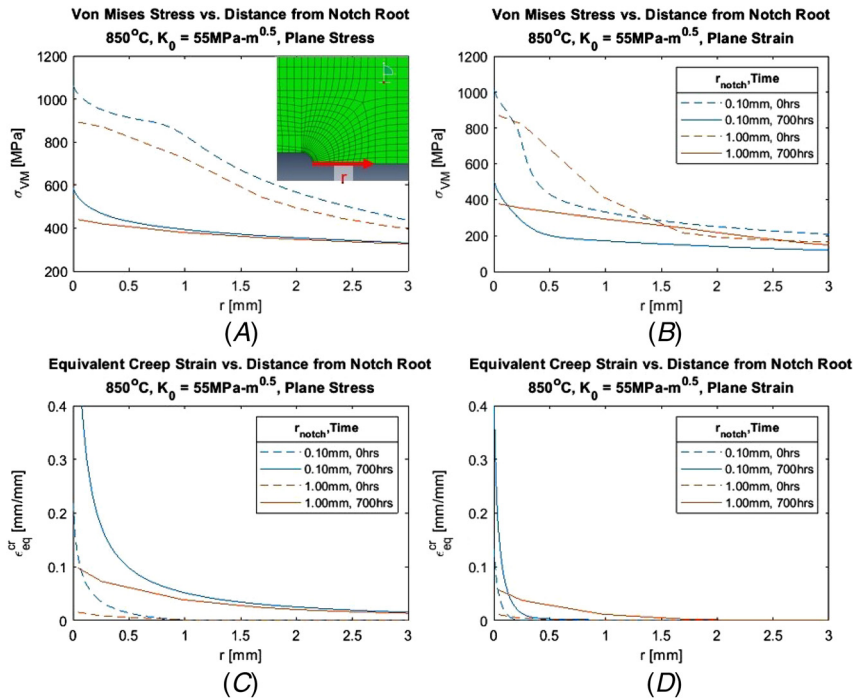
that there is a decrease in the load-line displacement rate with time. This decrease results from the creep zone evolving from small-scale creep conditions toward transition creep.

For a body subjected to creep, stress relaxation at the tip of a sharp crack[1–5] or a notch[21–23] has been reported. These observations were found to be applicable here as well. At each temperature studied and in both PS and PE conditions, reducing r_{notch} led to a steeper stress gradient ahead of the notch, a finding that aligned with Gallo, Berto, and Glinka.[23] The higher local stress results in higher local creep strain near the notch root with time. An example of these observations at 850°C is shown in figure 12 for the minimum and maximum notch root radius studied under PS and PE conditions.

Recall that the creep zone is the region where stresses relax due to creep deformation ahead of the tip of the crack or sharp notch. There are two definitions of the

creep zone size: (1) the locus of points where equivalent creep strain equals the equivalent elastic strain on the projected crack plane $(\theta=0°)$[1] and (2) the locus of points where equivalent creep strains equal 0.002 on the projected crack plane $(\theta=0°)$.[24] In this work, the differences in creep zone size based on these definitions were insignificant. This result is consistent with the observation of Adefris[24] when the creep exponent is much greater than 3, such as in this case. The first definition of creep zone size is used here to maintain consistency.

At each temperature studied, the size of the creep zone expanded with time, as expected. Figure 13A shows that a larger creep zone size develops in time for a more acute notch root radius for a given temperature and applied force under PS conditions. Conversely, under PE conditions, a larger creep zone size develops in time for a larger notch root radius, as shown in figure 13B. The cause of this difference can be explored by utilizing figure 12. Under PS conditions, figure 12A shows that the stress distribution ahead of the more acute notch has a larger region of influence compared to the larger notch. This leads to more creep accumulation over a larger area (fig. 12C) and thus a larger creep zone size. However, under PE conditions, figure 12B shows that outside of the local vicinity of the notch root, the stress distribution ahead of the larger notch root radius has a larger region of influence than a more acute notch, which results in a larger creep accumulation region (fig. 12D). Therefore, a larger creep zone size develops for the larger notch root radius in this situation. Clearly, stress state and notch tip acuity influence the development of the creep zone; therefore, limiting analyses solely to 2D PS or 2D PE FEA will be insufficient.

FIG. 13 Comparison of the creep zone evolution with time for various r_{notch} values for (A) PS conditions and (B) PE conditions. Crack formation occurred in the experiment ~700 hr. Note that the maximum plotted duration in (A) has been truncated because the creep zone size exceeded the probed edge length.
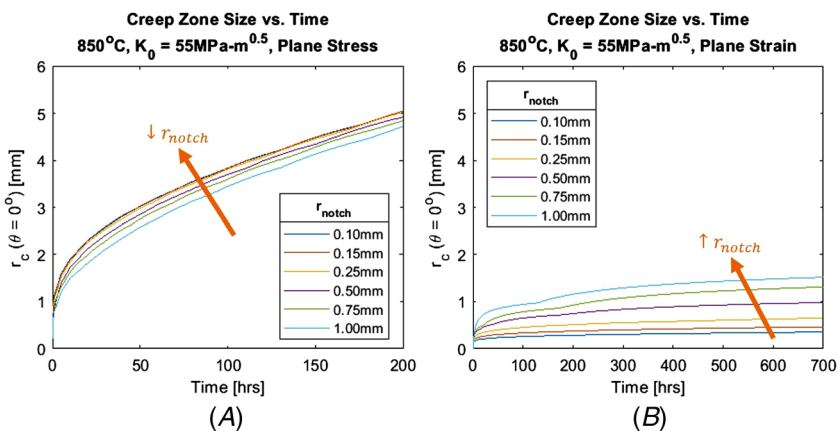
It is possible to understand how the notch geometry affects the development of the creep zone by reviewing the creep zone expansion rate with time, as shown in figure 14. Under PS conditions, the influence of the notch root radius on the development of the creep zone size diminishes in time. Figure 14A shows that the rate of change of the creep zone size for different notch root radii collapses along a single trend line after the creep zone size exceeds the radius of the notch. Therefore, it may be concluded that the notch geometry no longer influences the development of the creep zone at this point. This conclusion cannot be extended to the PE condition because the creep zone expansion rates do not collapse along a single trend line, as shown in figure 14B. It is also observed that the creep zone expansion rate under PE conditions is approximately an order of magnitude less than in PS conditions and decays faster in time.

Figure 15 shows how the evolution of the creep zone size with time compares between temperatures of 750°C and 850°C under PS and PE conditions for a given r_{notch} and applied force. Over long periods of time, the creep zone size at 850°C grows larger than at 750°C for both stress states. In essence, the higher temperature model is trending toward transition creep conditions more rapidly than the specimen at lower temperature. This can be expected because the transition time from small-scale creep conditions to extensive creep conditions is expected to be shorter at higher temperatures. Interestingly, at short times and under PS conditions (subplot in fig. 15A), a larger creep zone size is observed at 750°C than at 850°C. This is due to the initially dominant small-scale primary creep.

2D PS and PE models are limiting cases of the 3D nature of creep deformation. Figure 16 shows that the predicted evolution of the creep zone from the 3D model at the free surface and midplane of the model falls between these limiting cases, as expected. It is evident from the 3D finite element results that there are significant

FIG. 14 Comparison of the creep zone expansion rate for various r_{notch} values versus time for (A) PS conditions and (B) PE conditions.
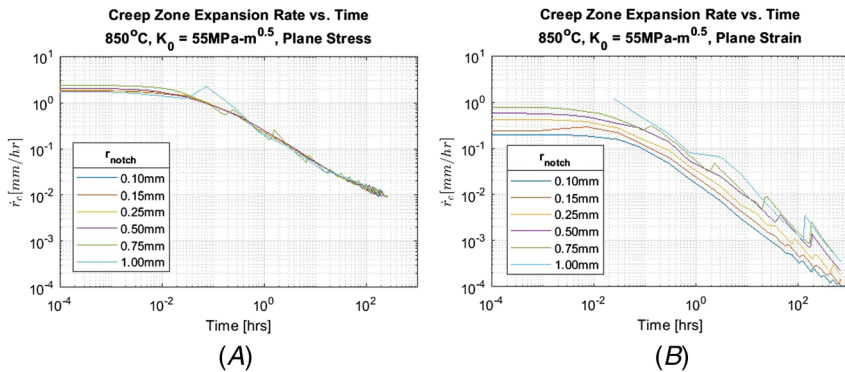
FIG. 15 Plot comparing creep zone size evolution across temperatures for a given notch root radius and applied force for (*A*) PS conditions and (*B*) PE conditions. Perturbations in the plots result from discretization of the models with a larger r_{notch} and are expected to disappear with additional mesh refinement.
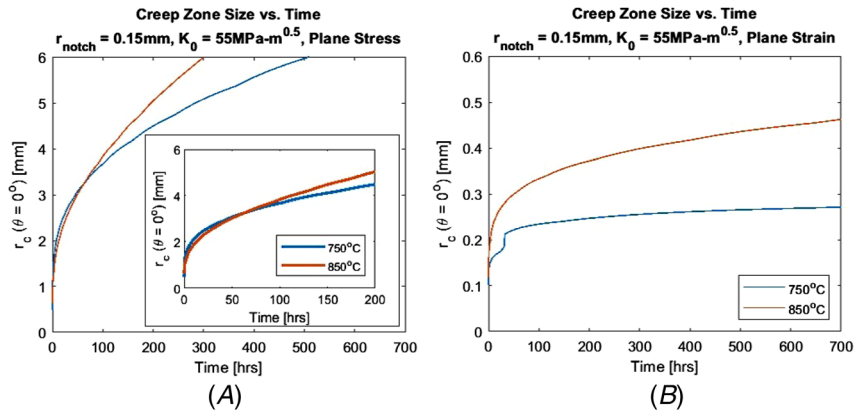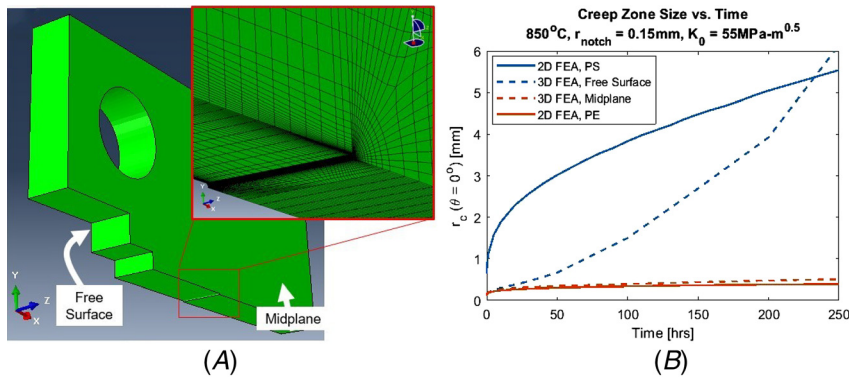

FIG. 16 (*A*) 3D model geometry with pertinent locations defined; (*B*) 2D versus 3D model comparison of creep zone evolution with time.

differences in the growth of the creep zone through the thickness of the sample at the tip of sharp notches, which cannot be neglected. The creep zone size on the surface and at the midplane of the sample is plotted with time in figure 17 for a notch root radius of 0.10 mm and 1.00 mm. It is seen that the creep zone size grows faster at the free surface than at the midplane of the sample for both notch root radii. The differences between the creep zone size at the surface and at the midplane are small initially but increase with time as the specimen transitions out of small-scale creep

FIG. 17   Variations in creep zone size evolution with time for the minimum and maximum notch root radii evaluated.
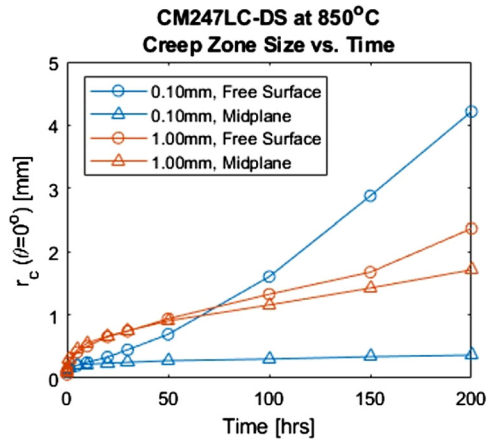
conditions. Furthermore, the differences are more pronounced in the sample with the sharper notch root radius of 0.10 mm than in the sample with a notch root radius of 1.00 mm. It is also observed that differences between creep zone sizes at the surface and at the midplane begin to occur at a significantly longer time for the 1.00-mm notch root radius sample than for the one with a notch root radius of 0.10 mm. This fact suggests that the stress gradient at the tip of a sharp notch is related to the uniformity of the creep zone evolution; a steeper stress gradient will lead to significant variation in creep zone size through the thickness. Furthermore, note that the larger r_{notch} yielded a larger creep zone size initially. This point may be explained by the stress concentration of the larger radius notch having a larger region of influence compared to the more acute notch.

Conclusions

Finite element analyses were performed for varying crack tip or notch geometries and temperatures in C(T) specimens of the Ni-base superalloy CM247LC-DS used in gas turbine blades to understand the accumulation of creep strains at notches. The constitutive models used considered elastic-primary-secondary creep deformation behavior, and the simulations were performed under 2D PS, 2D PE, and 3D conditions for temperatures of 750°C, 850°C, and 950°C. Good agreement between the experimentally measured load-line displacement rates and those calculated from FEA and analytical models was found, validating the FEA simulations.

Stress relaxation occurs, as expected, near the tips of sharp notches and cracks in CM247LC-DS Ni-base superalloy due to creep deformation. The creep zone size increases at a decreasing rate. Under PS conditions, the creep zone size grows

similarly for all notch root radii once it attains a size larger than the root radius of the notch. However, this conclusion does not hold under PE conditions. The evolution of the creep zone is significantly affected by the notch root radius before size of the creep zone is the same size as the notch root radius.

Under PS conditions, the creep zone sizes are seen to initially evolve at a higher rate at 750°C than at 850°C due to the presence of primary creep at 750°C. However, as time progresses, the creep zone size at 850°C exceeds the size at 750°C because secondary creep becomes the more dominant contributor to the creep zone deformation accumulation.

The 3D creep zone size differs from the simple 2D PS or PE bounding cases. Sharper notches cause the creep zone to develop more nonuniformly through the thickness of the sample than a blunter notch. Furthermore, this nonuniformity occurs earlier in time and at a much faster rate for a sharper notch.

The trends observed from the FEA simulations may be potentially used to formulate a theory of crack formation in a CM247LC-DS alloy, but prior to its formulation, the constitutive models must be adjusted to include the effects of creep anisotropy and an understanding of crack and microstructure interactions.

ACKNOWLEDGMENTS

References

1. H. Riedel and J. R. Rice, "Tensile Cracks in Creeping Solids," in *Fracture Mechanics* (West Conshohocken, PA: ASTM International, 1980).

2. J. L. Bassani and F. A. McClintock, "Creep Relaxation of Stress around a Crack Tip," *International Journal of Solids and Structures* 17, no. 5 (1981): 479–492.

3. F. Z. Li, A. Needleman, and C. F. Shih, "Characterization of Near Tip Stress and Deformation Fields in Creeping Solids," *International Journal of Fracture* 36, no. 3 (1988): 163–186.

4. D. S. Wilkinson and S. B. Biner, "Creep Crack Growth Simulation under Transient Stress Fields," *Metallurgical Transactions A* 19, no. 4 (1988): 829–835.

5. L. G. Zhao, J. Tong, and J. Byrne, "Finite Element Simulation of Creep-Crack Growth in a Nickel Base Superalloy," *Engineering Fracture Mechanics* 68, no. 10 (2001): 1157–1170.

6. K. Harris, G. L. Erickson, and R. E. Schwer, "MAR M 247 Derivations—CM247LC-DS Alloy and CMSX Single Crystal Alloys: Properties and Performance," in *Superalloys* (Muskegon, MI: Cannon-Muskegon Corporation, 1984).

7. G. L. Erickson, K. Harris, and R. E. Schwer, "Directionally Solidified DS CM 247 LC—Optimized Mechanical Properties Resulting from Extensive γ' Solutioning," in *Proceedings of the International Gas Turbine Conference* (Houston, TX: ASME, 1985).

8.   R. C. Reed, *The Superalloys: Fundamentals and Applications* (Cambridge, UK: Cambridge University Press, 2006).

9.   C. C. Engler-Pinto Jr., C. Noseda, M. Y. Nazmy, and F. Rezai-Aria, "Interaction between Creep and Thermo-Mechanical Fatigue of CM247LC-DS," in *Superalloys 1996: Proceedings of the Eighth International Symposium on Superalloys*. (Pittsburgh, PA: Minerals, Metals, and Materials Society, 1996).

10. M. Maldini, M. Marchionni, M. Nazmy, M. Staubli, and G. Osinkolu, "Creep and Fatigue Properties of a Directionally Solidified Nickel Base Superalloy at Elevated Temperature," in *Superalloys 1996: Proceedings of the Eighth International Symposium on Superalloys*. (Pittsburgh, PA: Minerals, Metals, and Materials Society, 1996).

11. *Standard Test Method for Measurement of Creep Crack Growth Times in Metals*, ASTM E1457-19 (West Conshohocken, PA: ASTM International, approved November 15, 2019), https://doi.org/10.1520/E1457-19

12. F. H. Norton, *The Creep of Steel at High Temperatures* (New York, NY: McGraw-Hill, 1929).

13. F. Garofalo, *Fundamentals of Creep and Creep-Rupture in Metals* (New York, NY: Collier-Macmillan, 1965).

14. H. Riedel, "Creep Deformation at Crack Tips in Elastic-Viscoplastic Solids," *Journal of the Mechanics and Physics of Solids* 29, no. 1 (1981): 35–49.

15. A. Saxena, *Advanced Fracture Mechanics and Structural Integrity* (Boca Raton, FL: CRC Press, 2019).

16. "Linear Elastic Behavior," Dassault Systemes, 2020, https://archive.org/details/linear-elastic-behavior-2020-dssimulia-established

17. "Rate-Dependent Plasticity: Creep and Swelling," Dassault Systemes, 2020, https://archive.org/details/rate-dependent-plasticity-creep-and-swelling-2020-dssimulia-established

18. S. D. Neal, *Reduced Order Constitutive Modeling of a Directionally-Solidified Nickel-Base Superalloy* (Atlanta, GA: Georgia Institute of Technology, 2013).

19. R. Darveaux and K. Banerji, "Constitutive Relations for Tin-Based Solder Joints," *IEEE Transactions on Components, Hybrids, and Manufacturing Technology* 15, no. 6 (1992): 1013–1024.

20. J. C. Newman Jr., "Stress Analysis of the Compact Specimen Including the Effects of Pin Loading," in *Fracture Analysis* (West Conshohocken, PA: ASTM International, 1974).

21. S. Kubo and K. Ohji, "Development of Simple Methods for Predicting Plane-Strain and Axi-Symmetric Stress Relaxation at Notches in Elastic-Creep Bodies," in *Proceedings of the International Conference on Creep* (Tokyo, Japan: JSME, 1986), 417–422.

22. J. E. Nunez and G. Glinka, "Analysis of Non-Localized Creep Induced Strains and Stresses in Notches," *Engineering Fracture Mechanics* 71, no. 12 (2004): 1791–1803.

23. P. Gallo, F. Berto, and G. Glinka, "Generalized Approach to Estimation of Strains and Stresses at Blunt V-Notches under Non-Localized Creep," *Fatigue and Fracture of Engineering Materials and Structures* 39, no. 3 (2016): 292–306.

24. N. Adefris, *Creep-Fatigue Crack Growth Behavior of 1Cr-1Mo-0.25V Rotor Steel* (Atlanta, GA: Georgia Institute of Technology, 1993).